China Geology 7 (2024) 203−221

China Geology

Journal homepage: http://chinageology.cgs.cn
https://www.sciencedirect.com/journal/china-geology

Deformation, structure and potential hazard of a landslide based on InSAR in Banbar county, Xizang (Tibet)

Guan-hua Zhao[a, b], Heng-xing Lan[b, c, d,*], Hui-yong Yin[a], Lang-ping Li[b, e,*], Alexander Strom[f], Wei-feng Sun[c], Chao-yang Tian[c]

[a] *College of Earth Science and Engineering, Shandong University of Science and Technology, Qingdao* 266590, *China*
[b] *State Key Laboratory of Resources and Environmental Information System, Institute of Geographic Sciences and Natural Resources Research, Chinese Academy of Sciences, Beijing* 100101, *China*
[c] *School of Geological Engineering and Geomatics, Chang'an University, Xi'an* 710054, *China*
[d] *Key Laboratory of Ecological Geology and Disaster Prevention, Ministry of Natural Resources, Xi'an* 710054, *China*
[e] *University of Chinese Academy of Sciences, Beijing* 100049, *China*
[f] *JSC "Hydroproject Institute", Moscow* 125993, *Russia*

ARTICLE INFO

Article history:
Received 8 November 2023
Received in revised form 6 January 2024
Accepted 11 March 2024
Available online 15 April 2024

Keywords:
Landslide
InSAR
Human activity
Deformation
Structure
LSTM model
Engineering construction
Thickness
Neural network
Machine learning
Prediction and prevention
Tibetan Plateau
Geological hazards survey engineering

ABSTRACT

The Tibetan Plateau is characterized by complex geological conditions and a relatively fragile ecological environment. In recent years, there has been continuous development and increased human activity in the Tibetan Plateau region, leading to a rising risk of landslides. The landslide in Banbar County, Xizang (Tibet), have been perturbed by ongoing disturbances from human engineering activities, making it susceptible to instability and displaying distinct features. In this study, small baseline subset synthetic aperture radar interferometry (SBAS-InSAR) technology is used to obtain the Line of Sight (LOS) deformation velocity field in the study area, and then the slope-orientation deformation field of the landslide is obtained according to the spatial geometric relationship between the satellite's LOS direction and the landslide. Subsequently, the landslide thickness is inverted by applying the mass conservation criterion. The results show that the movement area of the landslide is about 6.57×10^4 m^2, and the landslide volume is about 1.45×10^6 m^3. The maximum estimated thickness and average thickness of the landslide are 39 m and 22 m, respectively. The thickness estimation results align with the findings from on-site investigation, indicating the applicability of this method to large-scale earth slides. The deformation rate of the landslide exhibits a notable correlation with temperature variations, with rainfall playing a supportive role in the deformation process and displaying a certain lag. Human activities exert the most substantial influence on the spatial heterogeneity of landslide deformation, leading to the direct impact of several prominent deformation areas due to human interventions. Simultaneously, utilizing the long short-term memory (LSTM) model to predict landslide displacement, and the forecast results demonstrate the effectiveness of the LSTM model in predicting landslides that are in a continuous development and movement phase. The landslide is still active, and based on the spatial heterogeneity of landslide deformation, new recommendations have been proposed for the future management of the landslide in order to mitigate potential hazards associated with landslide instability.

1. Introduction

China has complex geological conditions and diverse topography. Mountainous areas account for about two-thirds of the country's land area. Consequently, geological such as landslides, mudslides, and collapses occur frequently, posing a significant threaten to human life and property (Ge DQ, 2018). Landslide refers to the natural phenomenon where a large quantity of rock, soil, and debris on a slope moves downward along the slope surface due to a combination of internal factors, such as geological strata and terrain, and external factors, including earthquakes, precipitation, and human activities. Internal factors such as rock types and fault

First author: *E-mail address*: zghua99@163.com (Guan-hua Zhao).
* Corresponding author: *E-mail address*: lanhx@igsnrr.ac.cn (Heng-xing Lan); lilp@lreis.ac.cn (Lang-ping Li).

Literary editor: Xi-jie Chen
doi:10.31035/cg2023130
2096-5192/© 2024 China Geology Editorial Office.

lines provide the fundamental material for landslides, while external factors such as earthquakes, precipitation, reservoir construction, and road building often trigger landslide disasters (Liao MS et al., 2017). The occurrence of landslide disasters poses a severe threat to people's lives and property (Froude MJ and Petley DN, 2018; Zhao CY and Lu Z, 2018). In recent years, destructive landslide events have significantly increased in China due to human activities and climate change (Chen XZ and Cui YF, 2017; Qiu HJ et al., 2017). For instance, in 2017, a large-scale landslide in Xinmo Village, Sichuan Province, China, resulted in the death of over one hundred people (Fan XM et al., 2017). In October and November of 2018, the Baige landslide in southwestern China experienced two instances of instability, leading to the formation of a barrier lake. Subsequent disaster chain events resulted in significant losses (Fan XM et al., 2019).

The Tibetan Plateau, known as the “Roof of the World”, is characterized by its complex geological conditions, high-altitude environment, and intricate ecosystems, which collectively render its ecological environment relatively fragile. In recent years, major infrastructure projects and new urban development have extended into the high mountain valleys of the Tibetan Plateau, posing an even greater threat to an already fragile ecological environment and leading to an increasing risk of landslides.

Landslide disasters on the Tibetan Plateau exhibit complex characteristics influenced by various factors. Firstly, landslides in this region often display intricate deformations. Over time, landslides tend to change in response to the environment. Secondly, they involve multiple layers of soil, rock, and ice, resulting in the complexity of the internal structure of the landslide mass. Lastly, due to the influence of mountainous terrain, the gentle topography formed by ancient landslides often serves as crucial areas for human activities. With the escalating intensity of human activities in recent years and the frequent occurrence of extreme events, the resurgence of ancient landslides has become a rapidly rising concern both domestically and internationally. This phenomenon has led to increasingly severe consequences, including casualties and economic losses (Sassa K et al., 2015; Zhang YS et al., 2020). Due to the high-altitude, concealed, and sudden nature of landslides in mountainous areas, disaster prevention and mitigation for landslides pose significant challenges (Zhu Q et al., 2019; Zhang YS et al., 2020). Early identification, monitoring, early warning, risk assessment and evaluation of landslides have become crucial tasks in the field of disaster prevention and mitigation (Zhao Z et al., 2021; Cao YM et al., 2022; Lan HX et al., 2022; Yao JM et al., 2022; Tian NM et al., 2022; Zhao Z and Chen JH, 2023b; Zhao Z et al., 2024).

In recent years, InSAR techniques have found wide application in landslide monitoring, especially for large and slow-moving landslides (Delacourt C et al., 2007). while ground-based techniques like differential GPS or GNSS (Coe JA et al., 2003) offer high accuracy and temporal resolution for direct landslide measurements, they are constrained by labor and resources limitations and have lower spatial resolution. InSAR offer a primary advantage with their higher spatial resolution. In the context of landslide monitoring, length, width, and aspect ratio are fundamental parameters extensively employed to describe the geometric characteristics of landslides. The aspect ratio reflects the overall extension of the landslide, which is related to the propagation of the landslide along its path of movement (Li LP et al., 2022). Combining landslide geometry and thickness characteristics allows for a more accurate landslide hazard analysis and risk assessment.

In this study, the authors have chosen a landslide in the Banbar county seat, Xizang, as a representative case to examine the impacts of complex predisposing and triggering factors on landslide deformation. Initially, the authors employed SBAS-InSAR technology to retrieval the Line of Sight (LOS) deformation characteristics of the landslide. Subsequently, the authors obtained deformation features along the slope-orientation direction based on a constructed two-dimensional coordinate system. The authors then combined the principle of mass conservation to invert the thickness of the landslide. Finally, the authors discussed the impact of constraints within the study on the development, evolution, and spatial heterogeneity of the landslide. And this study employed the widely-used Long Short-Term Memory (LSTM) neural network model to forecast the landslide displacement. Based on the results, the authors provided recommendations for the subsequent prevention and mitigation of the landslide.

2. Study area and data

2.1. Study area

The study area is situated to the east of Banbar County seat, along the right bank of the Maiqu River, a tributary of the upper Nu River. It is in close proximity to the Maiqu River and is easily accessible, with two roads passing through it. Human activities are notably evident in this region (Fig. 1 and Fig. 2). The regional geomorphology is characteristics by structurally eroded high-mountain terrain, with elevations ranging from 3700–5500 m. The relative elevation difference typically falls between 500 and 1800 m. The Banbar-Luolong fault zone, which is a left-slip fault, traverses the area (Fig. 1). Exposed geological strata in the landslide area mainly include Quaternary Neogene landslide deposits (Q_4^{del}), residual slope deposits (Q_4^{el+dl}), alluvial deposits (Q_4^{al+pl}), and the Jurassic-Cretaceous Jiega Formation (K_2j) (Fig. 2). The study area is situated between the Bangong Lake-Nu River suture zone and the Gangdise-Nyainqentanglha Range-Qiangtang-Sanjian Complex Plate. Recent tectonic movement is primarily characterized by vertical crustal uplift, tectonic development, rock joints, fissure development, and rock fragmentation, which form the fundamental geological basis for landslide formation.

The study area receives an average annual precipitation of 600 mm, which is unevenly distributed throughout the year. It

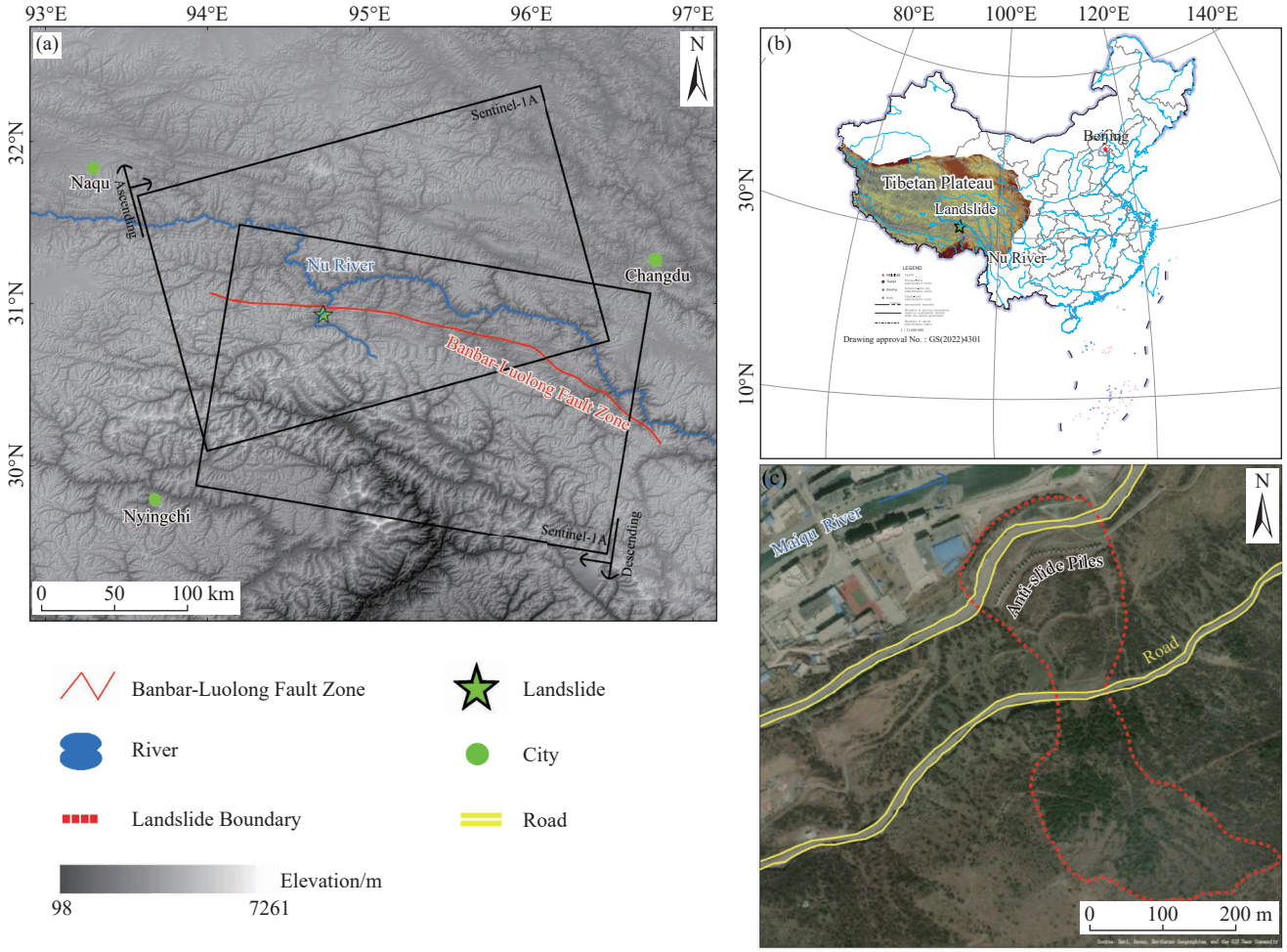

Fig. 1. Banbar landslide. a–Geographical location and SAR image coverage of the Banbar landslide. b–location of the study area in China. c-plan view of the landslide. Pentagram marks the location of the landslide area investigated in this study.

experiences distinct wet and dry seasons, with the rainy season typically occurring from June to September. This period aligns with both the rainy season and an increased concentration of geological hazard in the mountainous region. During this time, rainfall accounts for 85% of the total annual precipitation. The dry season extends from October to the following May, characterized by minimal precipitation. However, the substantial precipitation during the wet season serves as a significant trigger for landslide instability.

The overall terrain of the landslide area slopes from the southeast to the northwest, creating a stepped topography. The rear of the landslide mass exhibits a steep rock face with angles ranging from 50° to 80° and a height of 10 m to 20 m, which forms the rear boundary of the old landslide. The rear slope is relatively gentle with angles of 15° to 25°, while the middle part has steeper slopes ranging from 25° to 35°. The front slope is milder, with angles of 10° to 15°. The landslide material is primarily composed of purplish-red fragmented gravel soil, followed by blocky soil. The soil contains interlayers of clay and sandy gravel soil (Fig. 3). The longitudinal extent of the landslide body is thicker in the middle and rear sections, while it is thinner at the front. In the lateral direction, the landslide body is thicker in the middle and thinner on both sides. This landslide is classified as a large-scale earth slide (Yang G et al., 2021).

2.2. Data

This study utilizes a total of 217 Sentinel-1 SAR images provided by the European Space Agency (ESA. https://scihub.copernicus.eu) with a spatial resolution of 30 m to derive time series deformation histories. The specific data parameters are summarized in Table 1. Topographic and geological data are sourced from the shuttle radar topography mission (SRTM) and China Geological Survey, respectively. The daily precipitation and temperature data used in this study are independently obtained from NASA (https://pmm.nasa.gov) and NOAA (https://gis.ncdc.noaa.gov).

3. Methodology

Currently, the probing of landslide thickness mainly falls into two main categories: contact and non-contact methods. Among these, contact-based techniques for landslide thickness assessment include deep displacement measurement, which can be costly and time-consuming (Feng WK et al., 2017), and ground-penetrating radar (GPR) detection, suitable for shallower landslides but with relatively lower efficiency (Bichler A et al., 2004; He KS et al., 2005;

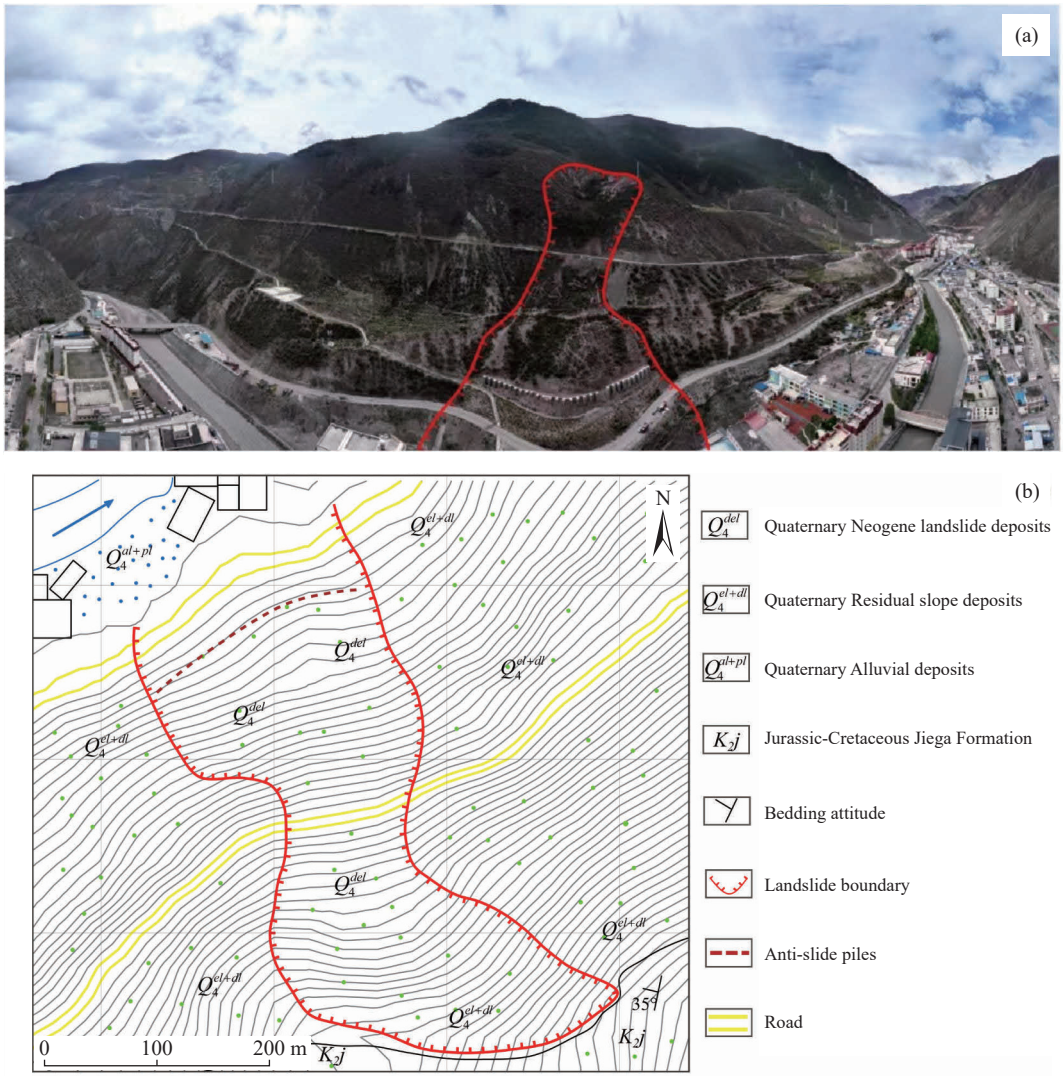

Fig. 2. a–Aerial wide-angle photo of the landslide in Banbar County captured by UAV. b–engineering geological plan of the landslide.

Yang YF et al., 2009). These methods pose challenges when applied to large or massive landslides and are impractical for landslides that feature steep and rugged terrain, difficult accessibility, and significant hazards.

Non-contact methods for detecting landslide thickness mainly include the balanced cross-section method (Bishop KM, 1999; Aryal A et al., 2015), the elastic dislocation method (Nikolaeva E et al., 2014; Aryal A et al., 2015), and the mass conservation method (Booth AM et al., 2013; Huang MH et al., 2017; Hu X et al., 2018). The balanced cross-section method, by neglecting the rheological properties of landslides materials, may result in limited reliability when estimating landslide thickness (Rowan MG et al., 1989; Zhang T et al., 2014). In contrast, the elastic dislocation method simplifies the landslide mass in terms of both geometric and physical models and is generally applicable only to the initial stages of landslides or cases where the landslide mass exhibits no pronounced non-elastic deformation (Feigl KL et al., 1999). The mass conservation method is a novel non-contact approach developed in recent years for calculating the thickness of deformation bodies such as glaciers and landslides (Rasmussen Lowell A, 1988; Farinotti D et al., 2009; Morlighem M et al., 2011), this method takes into full consideration the surface deformation characteristics of the slope and the rheological coefficients of the soil mass. It holds the potential to provide a reliable technical approach for non-contact landslide thickness inversion (Handwerger AL et al., 2021).

To utilize the mass conservation method for inferring landslide thickness, a three-dimensional surface deformation field of the slope is required (Hu X et al., 2016; Kang Y et al., 2023). However, existing research has shown that computing the two-dimensional and three-dimensional surface deformation of landslides by integrating ascending and descending satellite orbit data is highly feasible (Shi GL et al., 2022; Yang C et al., 2023; Zhu W et al., 2023). In this study, the authors utilized the SBAS-InSAR method to observe the Banbar landslide area, and the specific data processing flowchart is illustrated in Fig. 4.

3.1. LOS deformation retrieval

The landslide area is located in a mountainous region. Given the potential challenges related to coherence loss due to

Fig. 3. Photos of Banbar landslide. a–Overview of the study area captured by UAV and the specific locations of b, c, d, e, f, and g have been marked. d–east side of the front portion of the landslide captured by UAV. g–west side of the front portion of the landslide captured by UAV. c, f–cracking in houses near the front portion of the landslide. b, e– loose gravel soil behind the anti-slide piles.

Table 1. Parameters of Sentinel-1 SAR images of ascending and descending orbits.

Parameters	Orbit (Sentinel-1)	
	Ascending	Descending
Radar wavelength	5.6 cm	5.6 cm
Resolution	5×20 m	5×20 m
Repeat period	12 d	12 d
Incidence Angle	36.19°	44.37°
Scene Heading	347.28°	192.68°
Number	109	108
Date	2019.08.16–2023.06.20	2019.08.09–2023.06.25

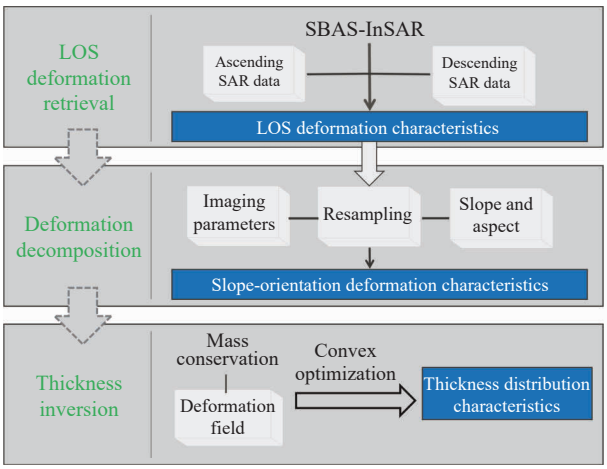

Fig. 4. Flowchart showing available data and methods used in this study.

long temporal baselines and the need to mitigate errors caused by atmospheric delays and terrain effects, the SBAS-InSAR technique offers distinct advantages for monitoring deformation in mountainous landslide areas. Thus, this study employed SBAS-InSAR technology to extract one-dimensional deformation information within the landslide area. Initially, SAR images were paired and clipped by using precise orbit determination (POD) provided by the European Space Agency, in combination with Digital Elevation Model (DEM) data, to generate a series of differential interferograms. By setting the temporal and spatial baseline thresholds of 60 days and 280 m, a total of 434 interferometric pairs were generated from 108 ascending SAR images. When the temporal and spatial baseline thresholds were set at 60 days and 288 m, 449 interferometric pairs were generated from the 109 descending SAR images. The generated interferometric pair information is displayed in Fig. 5. The study applied the Goldstein method for adaptive filtering of differential interferograms, thereby enhancing the quality of interferometric data. Phase unwrapping was accomplished using the Minimum Cost Flow method. An atmospheric filter was used to mitigate atmospheric phase contributions, followed by the application of singular value decomposition (SVD) to derive the temporal deformation of target points. Finally, the resulting data was geocoded to produce a time series deformation result within the landslide area.

3.2. Deformation decomposition

Time-series InSAR technology can measure the deformation as the projection of true three-dimensional ground displacement along the LOS. In complex high mountains and canyon areas with significant variations in slope and aspect, InSAR methods exhibit varying sensitivity

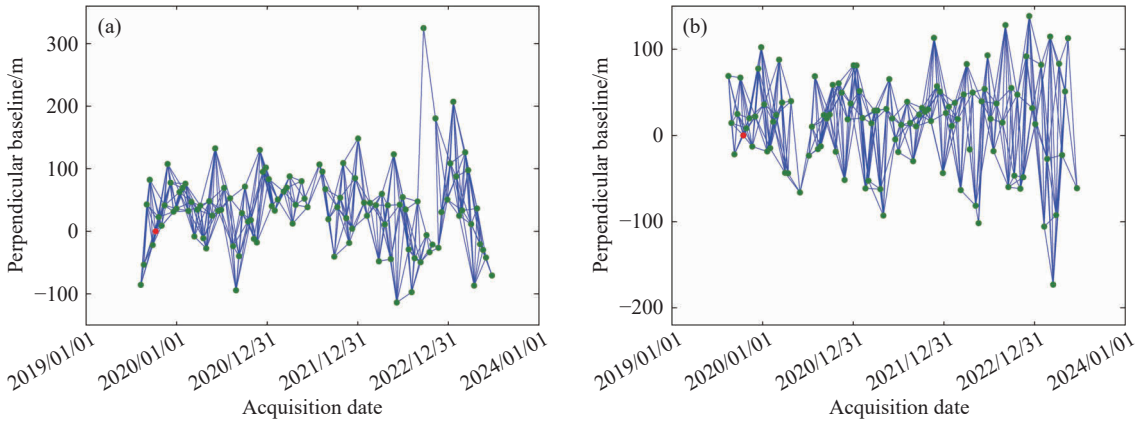

Fig. 5. Spatial and temporal baselines of the interferograms. a–ascending data. b–descending data. The red dots represent master images.

to deformation measurement due to different terrains. Thus, assessing deformation levels across diverse terrains cannot be solely reliant on a single LOS deformation velocity. To accurately describe actual ground deformation, slope and aspect are two fundamental factors. Slope characterizes the steepness of the ground surface, influencing the intensity of material flow on the surface. Given the anisotropy of terrain, the slope of a specific point varies in different directions, thereby rendering slope directional. The direction of the greatest terrain descent is the aspect of that point. When a landslide mass descends along the sliding surface under natural forces, due to the influence of elevation differences, the displacement primarily occurs in the direction of the aspect. Therefore, the coordinate system of the landslide sliding surface established in this study is based on the consideration of these two factors. It is important to note that, in practical scenarios, the sliding surface of a landslide often takes on an unknown and variable shape. Therefore, a homogeneous sliding surface is employed as a substitute for the actual sliding surface in this study (Booth AM et al., 2013; Shi GL et al., 2022; Yang C et al., 2023; Zhu W et al., 2023).

As shown in Fig. 6, when the landslide mass moves downward along the sliding surface, the sliding surface is composed of three unit orthogonal vectors: the aspect axis (OK), the perpendicular aspect axis (OT), and the normal axis (OI). The direction indicated by the aspect axis represents the aspect direction of the sliding surface, and the direction indicated by the normal axis represents the normal direction of the sliding surface. The authors define downward movement along the aspect axis as positive, rightward movement along the perpendicular aspect axis as positive, and upward movement along the normal axis as positive. Meanwhile, the LOS deformation can also be expressed using a "North-East-Up" coordinate system, defined by three directions: North-South (ON), East-West (OE), and vertical (OH). Thus, the geometric relationship between these two coordinate system can be established (Shi GL et al., 2022).

As Fig. 6 shown, the geometric relationship between the sliding surface and "North-East-High" coordinate system is depicted. D_K, D_T and D_I respectively represent the deformation components along the OK, OT and OI axis in the sliding surface coordinate system, while D_N, D_E and D_H denote the deformation components along the ON, OE and OH axis in the "North-East-High" coordinate system. α and β respectively represent the slope and aspect of the sliding surface. According to the geometric configuration shown in the figure, both D_K and D_I exhibit deformation projections in both the horizontal surface and the vertical direction. Due to the fact that the aspect axis OK and the normal axis OI are situated in the same vertical surface, the deformation projections of D_K and D_I in the horizontal surface should overlap. Meanwhile, D_T is perpendicular to the plane OPK, resulting in zero deformation projection in the vertical direction. D_T, located within the horizontal surface, manifests deformation projections in both the East-West and North-South directions. From this, the authors derive the projection relationship matrix between deformation in the sliding surface coordinate system and the "North-East-High" coordinate system, as follow:

$$\begin{bmatrix} D_E \\ D_N \\ D_H \end{bmatrix} = \begin{bmatrix} \cos\alpha\sin\beta & -\cos\beta & \sin\alpha\sin\beta \\ \cos\alpha\cos\beta & \sin\beta & \sin\alpha\cos\beta \\ -\sin\alpha & 0 & \cos\alpha \end{bmatrix} \begin{bmatrix} D_K \\ D_T \\ D_I \end{bmatrix} \quad (3\text{-}1)$$

This study acknowledge that the deformation in the LOS direction of radar satellites (D_{LOS}) is essentially the sum of deformation in the East-West direction (D_E), North-South direction (D_N), and vertical direction (D_H), all projected onto the LOS direction. Simultaneously, the authors define the direction toward satellite motion as positive, and the direction away from satellite motion as negative. Therefore, the authors can get:

$$D_{LOS} = \begin{bmatrix} \cos\theta\sin\theta\sin\varphi & -\sin\theta\cos\varphi \end{bmatrix} \begin{bmatrix} D_H \\ D_N \\ D_E \end{bmatrix} \quad (3\text{-}2)$$

In the equation, θ represents the incidence angle of the satellite, and φ represents the heading angle of the radar satellite.

From the above two equations, the authors can derive the projection relationship matrix between deformation in the sliding surface and the LOS of the radar satellite, as follows:

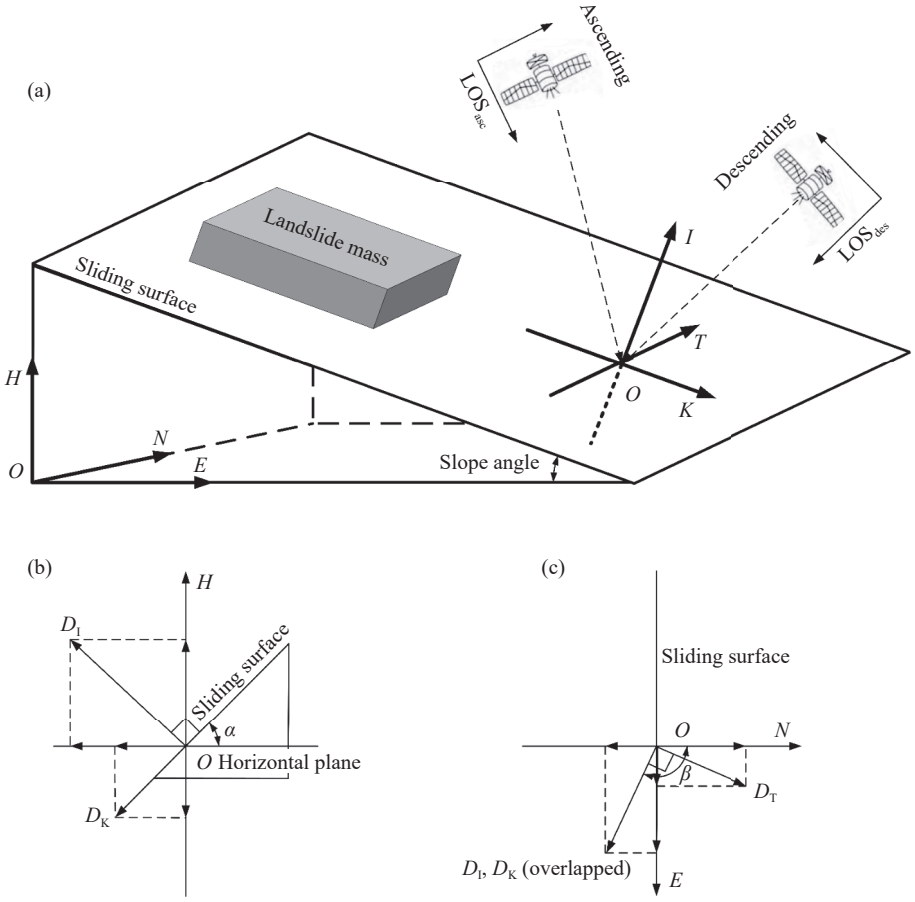

Fig. 6. Landslide deformation decomposition. a–coordinate system of the sliding surface of landslide, where ON represents North-South, OE represents East-West, OH represents Vertical. And on the sliding surface, OI represents normal, OT represents perpendicular and OK represents average aspect. b, c–geometric relationship between the sliding surface and "North-East-High" coordinate system.

$$\begin{cases} D_{LOS} = \begin{bmatrix} a & b & c \end{bmatrix} \begin{bmatrix} D_K \\ D_T \\ D_I \end{bmatrix} \\ a = \cos\theta\cos\alpha\sin\beta + \sin\theta\sin\varphi\cos\alpha\cos\beta + \\ \quad \sin\theta\cos\varphi\sin\alpha \\ b = -\cos\theta\cos\beta + \sin\theta\sin\varphi\sin\beta \\ c = \cos\theta\sin\alpha\sin\beta + \sin\theta\sin\varphi\sin\alpha\cos\beta - \\ \quad \sin\theta\cos\varphi\cos\alpha \end{cases} \tag{3-3}$$

In the equation, a, b, and c respectively represent the coefficients for the projections of deformation along the slope, perpendicular to the slope, and normal to the slope. Joint ascending-descending orbit imagery can only be used to calculate slope-orientation deformation data. Considering that when a landslide mass moves downhill, the magnitude of the velocity in the direction of the slope is much greater than the velocity in the direction perpendicular to the slope, therefore, equation (3-3) can be transformed into the following form:

$$\begin{cases} D_{LOS} = \begin{bmatrix} a & c \end{bmatrix} \begin{bmatrix} D_K \\ D_I \end{bmatrix} \\ a = \cos\theta\cos\alpha\sin\beta + \sin\theta\sin\varphi\cos\alpha\cos\beta + \\ \quad \sin\theta\cos\varphi\sin\alpha \\ c = \cos\theta\sin\alpha\sin\beta + \sin\theta\sin\varphi\sin\alpha\cos\beta - \\ \quad \sin\theta\cos\varphi\cos\alpha \end{cases} \tag{3-4}$$

The establishment of the aforementioned model relies on the assumption that there is no deformation perpendicular to the aspect direction of the sliding surface. This assumption corresponds to the deformation characteristics of the current landslide. Therefore, the model presented in this study may not be applicable to other types of landslides, such as translational landslides. Thus, in practical applications, it is crucial to ensure that the selected model aligns with the kinematic characteristics of the research objective.

3.3. Landslide thickness inversion

In this study, the authors use the mass conservation equation and the slope-orientation surface deformation field calculated in section 3.2 to invert the landslide thickness. The technique only needs surface change data and the simple assumption that the landslide's depth-averaged velocity is a spatially constant fraction of the observed surface velocity (Booth AM et al., 2013). So, for a landslide with constant density, mass conservation means that:

$$\frac{\partial h}{\partial t} = -\nabla \cdot (\bar{u}h) \tag{3-5}$$

In this equation, h represents the thickness of the landslide, t represents time, and $\bar{u}$ represents the depth-averaged horizontal landslide velocity vector. Since the

authors can measure surface velocity by InSAR technology, this study can make a simplifying assumption that:

$$\overline{u} = f u_{surf} \tag{3-6}$$

Where u_{surf} is the surface horizontal velocity vector and f is a constant between 0 and 1 that depends on landslide rheology. Due to the often difficult-quantify heterogeneous material properties of landslides, defining f as a constant implies that the rheology of the landslide is spatially homogeneous. Therefore, changes in thickness correspond solely to variations in the surface deformation filed. At the same time, define that:

$$f = \frac{2 - \frac{Y}{P}}{3} \tag{3-7}$$

Where Y and P respectively represent the thickness of the lower yield zone and the upper sliding zone. The rheological parameter f is employed to characterize the rheologial properties of soil, specifically the deformation behavior of soil under external forces, which signifies its shear resistance. According to the principles of power-law rheology, when f = 2/3, it indicates that the material behaves as a Newtonian viscous fluid, implying that the entire depth region from the slope surface to the sliding surface has yield, and the sliding zone disappears. When $2/3 < f < 1$, it signifies sliding zone, where the yield zone is relatively thin. When $f = 1$, it implies that the entire slope is a rigid block without a yield zone (Booth AM et al., 2013). Assuming that the reference surface of the landslide remains unchanged over a short period of time, equation (3-5) simplifies to:

$$\frac{\partial z}{\partial t} = -\nabla \cdot (f u_{surf} h) \tag{3-8}$$

In this equation, z represents the land surface elevation. In this study, $\partial z/\partial t$ and u_{surf} can be calculated by deformation decomposition. Equation (3-8) can be approximated as a finite difference grid and expressed as a system of N linear equations of the form:

$$Ah_f = b \tag{3-9}$$

Where N is the number of pixels in the velocity and elevation change grids, A is a diagonally matrix that includes surface velocity, $h_f = fh$ is a vector of the unknown thickness which scaled by f, and b is a vector containing elevation change data. In this study, the rheological parameter f is utilized to constrain the estimated model thickness. The objective is to emphasize the influence of rheology on thickness prediction, and conversely, to infer the impact of thickness on rheology through existing measurements. Consequently, different values of f correspond to different thickness models, despite each model sharing the same spatial pattern, with a magnitude that scaled as f^{-1}. In this research, the authors will determine the optimal match between measured values and predicted thickness based on several independent measurements. In practical solving processes, due to directional problem, the inverse problem may become ill-posed. Therefore, introducing L2 regularization to address this ill-posed problem helps find stable and meaningful results.

$$\left\| Ah_f - b \right\|^2 + \varepsilon^2 \left\| \nabla^2 h_f \right\|^2 \tag{3-10}$$

In this equation, double brackets indicate the Euclidian norm, and ε represents a damping factor, and introducing a damping factor in convex optimization problems can, to some extent, enhance numerical stability and convergence of the optimization problem. This is achieved by adding a regularization term to the objective function to control the smoothness of the final solution and mitigate numerical instability. This study use CVX (CVX Research, Inc., 2013), a program to solve convex optimization problems, to find h_f that minimizes expression (3-10) subject to the constraints that $h \geqq 0$ everywhere and that $h \approx 0$ on stable terrain.

4. Results

4.1. LOS deformation characteristics

This study conducted field surveys and obtained remote sensing images to approximate the extent of the landslide. SBAS-InSAR technology was utilized to retrieve the radar LOS deformation velocity field of the landslide area, as shown in Fig. 7. Fig. 7 illustrates that the rear part of the landslide is relatively narrow, whereas the front part is broader. The elevation of the landslide's front edge is approximately 3746 m, exhibiting an overall negative deformation rate, indicating movement away from the satellite direction, i.e., a subsurface and downstream shift towards the Maiqu River, a major tributary of the Nu River. The elevation of the landslide's rear edge is approximately 3958 m, with a height difference of about 212 m, showing a relatively slow deformation rate compared to the front edge. There are significant spatial and magnitude differences in the InSAR ascending and descending deformation fields of the landslide area. Specifically, the ascending deformation rate varies between −11 mm/a to 1 mm/a, with a maximum difference of 12 mm/a, while the descending deformation rate varies between −35 mm/a to 5 mm/a, with a maximum difference of 40 mm/a. Based on the deformation monitoring results from ascending and descending orbits, strong deformation areas i and ii are delineated separately (Fig. 7). It is clear from Fig. 8 that the maximum cumulative deformation of the ascending orbit in area i during the monitoring period is 42 mm, while in area ii, the maximum cumulative deformation of the descending orbit during the monitoring period is 128 mm.

In Fig. 7, it be observed differences in the deformation results obtained from ascending and descending orbit SAR images. Several factors contribute to these variations in InSAR deformation between ascending and descending orbits. Firstly, differences in observation direction, incidence angle, and azimuth angle of radar satellites lead to discrepancies in deformation results at the same location on the Earth's

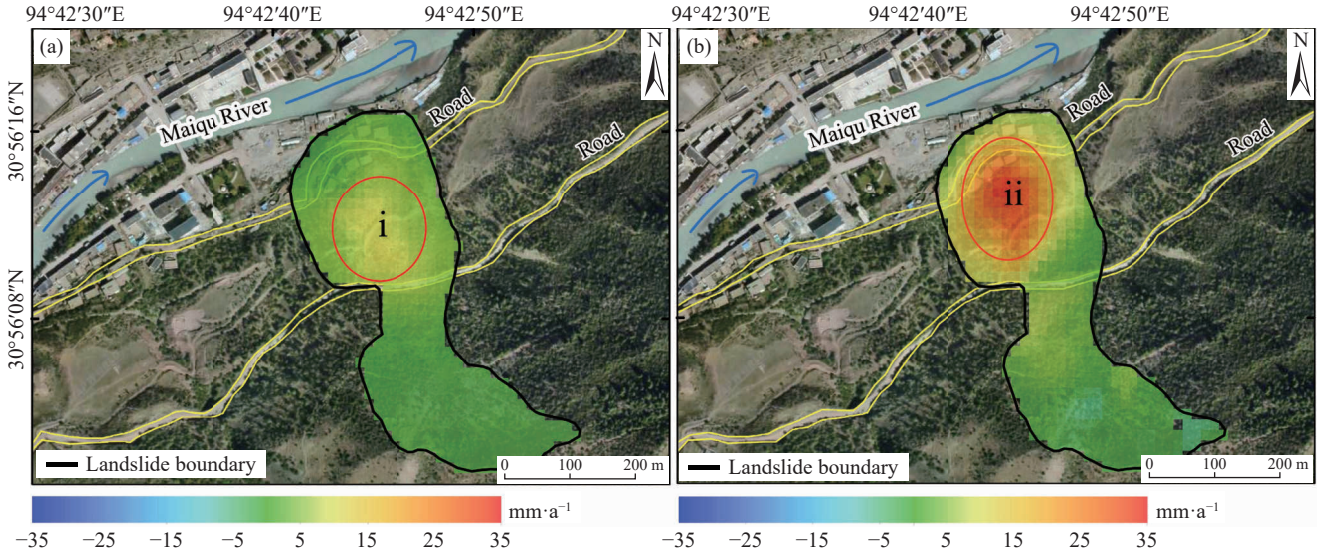

Fig. 7. Deformation velocity fields along the LOS. a–Ascending orbit of the landslide area. b–Descending orbit of the landslide area. i and ii are areas with higher deformation velocity.

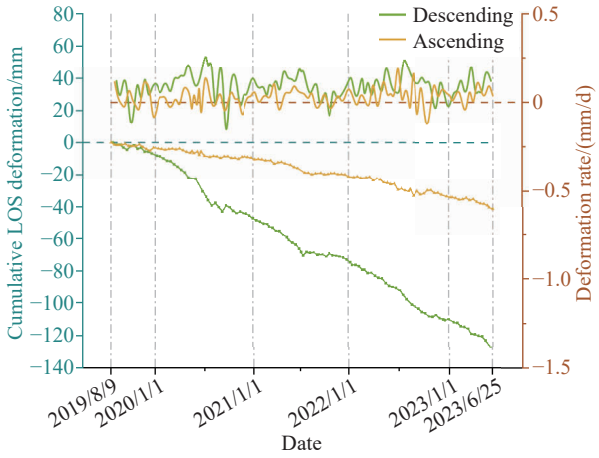

Fig. 8. Cumulative LOS deformation and deformation rates. The green dashed and solid lines represent the cumulative deformation value and deformation rate of the maximum deformation point in the descending orbit result, respectively. The yellow dashed and solid lines represent the cumulative deformation value and deformation rate of the maximum deformation point in the ascending orbit result.

surface. Secondly, in mountainous areas with significant topographical variations, SAR images may exhibit varying degrees of geometric distortion, directly impacting SAR observation data. Thirdly, in landslide monitoring using ascending and descending orbit images, there is varying sensitivity to landslide with different orientations. In general, descending SAR images exhibit higher sensitivity to landslides facing west, while ascending SAR images exhibit higher sensitivity to landslide facing east (Cigna F et al., 2014; Sun Q et al., 2016; Zhou L et al., 2017; Kovács IP et al., 2019; Esposito C et al., 2019; Dai KR et al., 2021).

Based on the sensitivity of ascending and descending orbit SAR images to landslides of different orientations, it is evident that descending orbit images exhibit higher sensitivity in studying landslides. Consequently, a careful observation of Fig. 7 reveals that significant deformation velocities are concentrated in area ii, corresponding to the vicinity of the landslide near the river and residential areas. The deformation appears to emanate outward from this region as the deformation center. While ascending orbit images exhibit lower sensitivity, they also reflect this characteristic. Although other areas within the landslide area exhibit relatively weaker deformation rates, they are all in an active state of deformation. Through on-site investigation, the authors have observed prominent deformation features of the landslide, primarily manifested by cracking of building and walls at the front edge of the landslide. Deformation activity is most active in the front portion of the landslide. Despite local measures such as constructing anti-slide piles to mitigate the subsequent impacts of the landslide, the presence of two roads crossing the landslide area and some human activities and engineering disturbances have still had an influence on the landslide. These field observations align with the characteristic depicted in Fig. 7 and Fig. 8, providing strong validation for the reliability of the InSAR deformation results obtained in this study. Furthermore, in Fig. 8, it can be observed that the deformation rate curves of the descending and ascending orbits exhibit a high degree of similarity, with the majority of the rate values remaining consistently above zero, indicating continuous cumulative deformation of the landslide. The fluctuations in deformation rate curves reveal that the landslide's deformation is influenced by various constraints.

4.2. Slope-orientation Deformation Characteristics

By employing the slope coordinate system and combining it with LOS deformation results, the slope-orientation deformation field along the slope of the landslide area was derived using equations (3-1) to (3-4), as shown in Fig. 9. From Fig. 9, it is evident that the slope-orientation deformation field obtained by decomposing along the slope is in close agreement with the LOS deformation distribution,

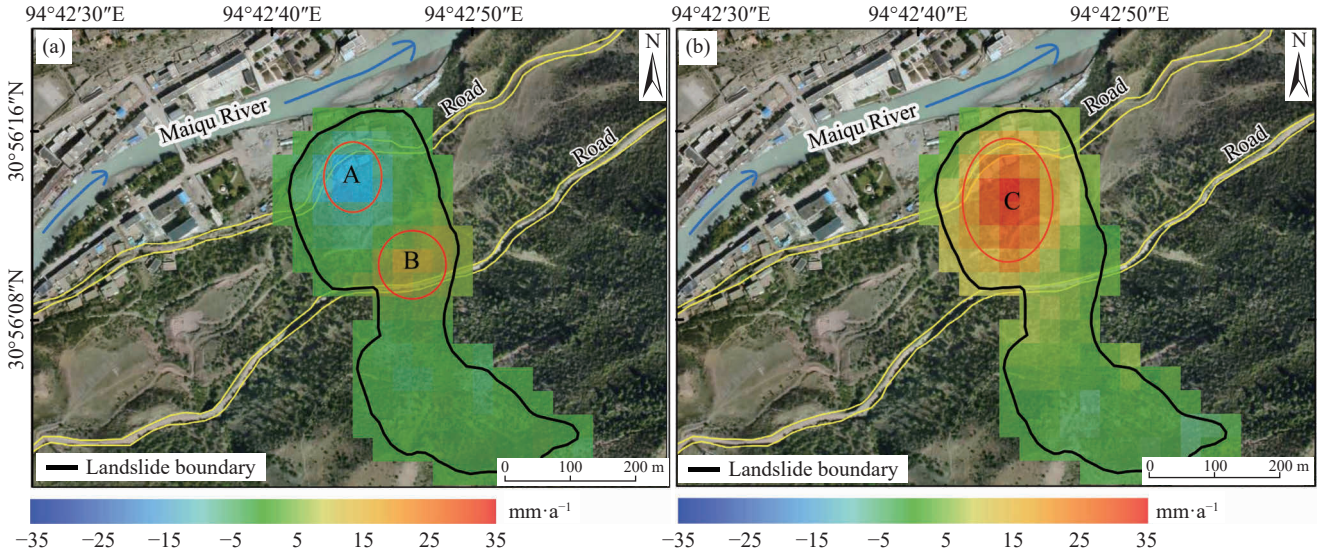

Fig. 9. Slope-orientation deformation velocity fields of the landslide. a–slope normal direction. b–slope direction. A and B are high deformation velocity areas with opposite directions. C is area with higher deformation velocity.

effectively portraying the movement intensity and direction of different areas within the landslide. The landslide deformation is primarily dominated by along-slope deformation, ranging from −5 mm/a to 34 mm/a, while deformation in the along-slope normal direction is relatively small, varying between −11 mm/a and 7 mm/a. Based on the magnitude and direction of deformation, significant deformation areas within the landslide are divided into area A, B, and C as shown in Fig. 9. Although along-slope deformation predominates over the landslide as a whole, significant deformation in the normal direction indirectly reflects a greater thickness of activity in these areas. Therefore, regions A and B can reflect that during the observation period, the landslide in these two areas had a greater thickness of activity.

As previously defined, with downward direction considered positive along the slope, the results shown in Fig. 9 imply that significant deformation area C as a whole is moving toward the river, aligning with on-site observations. The analysis reveals that the main deformation of the landslide is concentrated in the front part of the landslide mass. The front edge of the landslide is directly eroded by the river, which provides favorable aerial conditions for instability. Additionally, the elevated topography created by road excavation on the slope and building excavation at the front edge weakens the stability of the landslide mass, further increasing the possibility of landslide instability.

4.3. Thickness distribution

Prior research provided an approximate average thickness of the landslide, indicating an average thickness of about 30 m and a landslide volume of approximately 1.8×10^4 m^3 through drilling and deep-seated displacement monitoring. Additionally, thickness measurements were obtained at points b and c (Fig. 10 and Fig. 11). However, previous work did not quantitatively predict the entire three-dimensional underground geometry of the landslide. Previous work

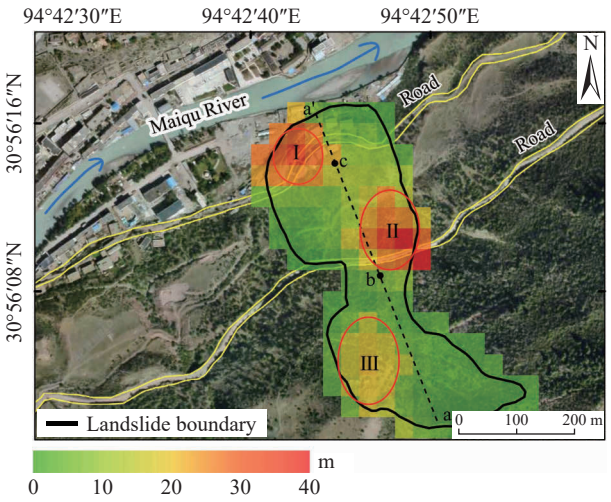

Fig. 10. Thickness distribution of landslide. I, II, and III are areas with relatively high prediction thickness values.

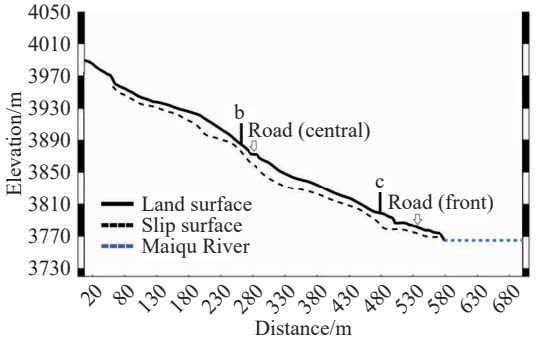

Fig. 11. Distribution of landslide thickness along profile aa'. b and c are monitoring points for deep-seated displacement (the actual values of landslide thickness at points b and c are known).

identified the presence of deep-seated sliding surface primarily located at the base-rock interface, where the sliding material consists mainly of fragmented rocky soil exhibiting hard-plastic or firm-plastic characteristics. There are also

shallower secondary sliding surfaces within the landslide body, composed of plastic to soft-plastic fine-grained clay interbedded with fragment rocks. These form weak interlayers that potentially serve as sliding surfaces within the landslide body. Notably, the shallower sliding surfaces exhibit significant displacement (Yang G et al., 2021). The authors used these inferences and measurements to evaluate the performance of thickness inversion. Simultaneously, the existing local thickness measurements at b and c were utilized to constrain the rheology by selecting f that minimizes the misfit between the inversion-predicted and measured thicknesses at these locations.

Using the constructed slope-orientation deformation field and the objective function (3-10) within the CVX system, this study obtained the optimal thickness prediction model (Fig. 10). According to the prediction model, the sliding surface of the landslide typically exhibits an upward concavity, with a maximum thickness of 39 m, which is roughly consistent with the previously estimated maximum thickness of 46.2 m. It's essential to mention that, based on the deep-seated displacement monitoring results, the authors determined that the actual thickness at b and c (Fig. 11) is approximately 8 m and 18 m, respectively. Using these two known results, the authors continuously adjusted the value of f within the CVX system to maximize the match between the predicted results and the actual results. Ultimately, when the predicted values at b and c were approximately 11 m and 19 m, respectively, the misfit from the actual results was minimized. This thickness model assumes $\varepsilon = 0.5$ and $f = 0.7$, which minimizes the misfit between thickness model and the thickness information obtained in previous work. Based on the results, the predicted average thickness of the landslide is approximately 22 m, which deviates somewhat from the measured average thickness of 30 m. It should be noted that this study obtained results represent the active thickness of the landslide during the observation period.

For ε, as long as it is less than 1, it does not strongly influence the volume estimation, as its primary role is to control the smoothness of the thickness model rather than the average thickness. The landslide volume is highly sensitive to f because this constant directly scales the predicted thickness magnitude.

The rheological parameter f represents the material's rheological characteristics, which include the compressibility and stability of the landslide material. When $f \leqq 0.5$, the landslide body can be regarded as a combination of granular flow or forward tilting and basal sliding, both of which indicate internal shear deformation within the landslide body. At this point, the soil compressibility within the slope is higher, the overall stability of the landslide is lower, and the probability of instability is greater. As the f increase, soil compressibility decrease, and when it approaches 1, the landslide body gradually approaches rigid behavior (Booth AM et al., 2013). The Quaternary loose deposits in the study area mainly consist of gravelly fine-grained clay, gravelly soil, followed by blocky soil, and gravelly pebble soil. The deposits are characterized by significant thickness, non-uniform particle size distribution, poor sorting, and loose structure. Based on the cumulative deformation time-series curve shown in Fig. 8, it can be inferred that the current landslide is most likely in a stable deformation phase and not in an imminent sliding state. Therefore, considering the geological structure of the landslide area and the deformation monitoring results, the authors can conclude that f value obtained through inverse analysis is consistent with the actual conditions of the landslide, further confirming the reliability of the results.

According to the landslide prediction result (Fig. 10), the current active volume of the landslide is estimated to be approximately 1.45×10^6 m^3. Based on the forecast results, three areas have been delineated: Area Ⅰ, area Ⅱ, area Ⅲ, which are the three areas with greater thickness. The maximum predicted thickness in these areas is approximately 30 m, 39 m, and 15 m, respectively. Overall, the distribution of landslide thickness shows a certain correlation with the slope-orientation deformation field of the landslide (Fig. 9).

Along the axis of the landslide, a cross-sectional aa' (as shown in Fig. 10) is taken to create a predictive thickness model for the landslide along the profile line (Fig. 11). The profile line aa' intersects through areas Ⅰ, Ⅱ, and Ⅲ. From Fig. 11, it can be observed that the thickness at the front and rear ends of the profile line is essentially 0 m. As it passes through the three areas, the thickness gradually increases and then slowly decreases as it proceeds towards the rear, presenting an overall concave sliding surface.

The constant f in the objective function represents the rheological coefficient of the landslide. It is clear that using a single constant to represent the overall condition of the landslide is inadequate. To adequately constrain both landslide rheology and thickness at all other locations within the landslide, the resulting failure plane model is calibrated to match one or more local, direct thickness measurements. In other words, the more direct observational data we have, the more accurate calibration results will be, leading to higher precision. However, in this study, the authors estimated the entire landslide thickness based on only two existing depth data points, which may have a certain impact on the accuracy of the calculations. Nevertheless, the obtained results do not significantly deviate from those obtained in previous field surveys, indicating that predictive models (Booth AM et al., 2013) can still reveal its geometric shape even in cases where little is known about a landslide. If further drilling is conducted to obtain local thickness or shallow geophysical techniques are employed, spatial constraints can be imposed, leading to favorable outcomes.

5. Discussion

5.1. Constraints of landslide overall deformation

Fig. 12 illustrates the relationship between the deformation rates of the maximum deformation points in both the descending and slope direction and the precipitation and

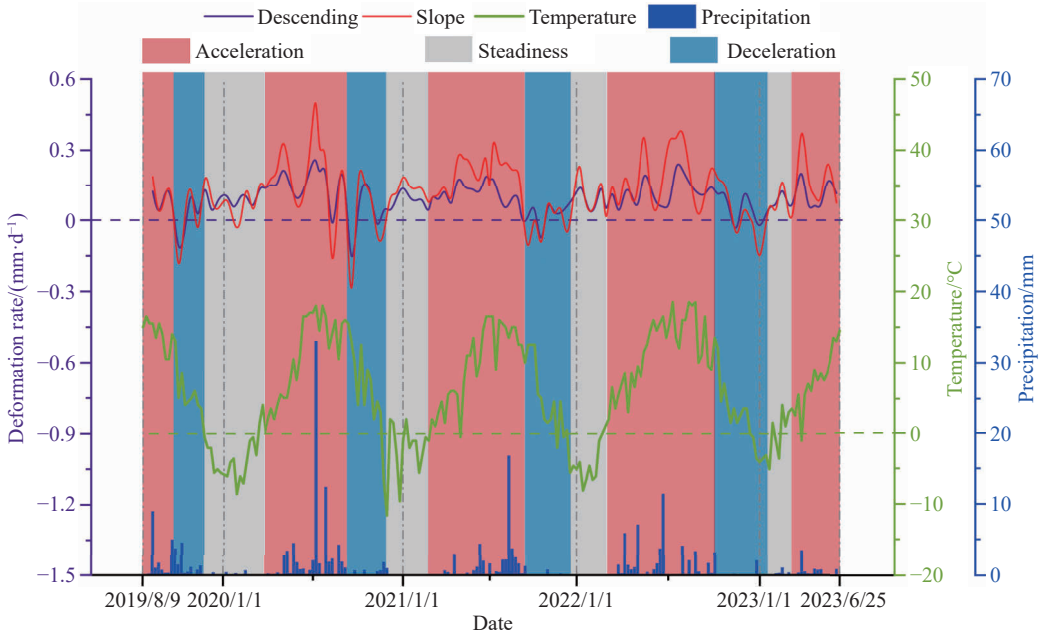

Fig. 12. Constraints data of landslide. The red curve and the purple curve respectively represent the deformation rate of the maximum deformation point in the slope deformation result and the deformation rate of the maximum deformation point in the descending orbit result. The dark green dashed line represents temperature, and the blue bar graph represents precipitation.

temperature in the study area. Overall, there is a noticeable similarity in the deformation rates and the temperature variations, exhibiting a certain degree of periodicity. Over the five years of observation, the temperature in the landslide area exhibited a stable fluctuation pattern with few instances of extreme high or low temperatures, following a seasonal variation with high temperatures in summer and lower temperatures in winter. Therefore, the deformation rates also exhibited a pattern of acceleration during summer and deceleration during winter in conjunction with temperature variations. Precipitation reached its peak in the summer of 2020, with a single-day maximum of 33 mm, while in the other years, precipitation showed relatively stable fluctuations, with the maximum annual precipitation consistently occurring in the summer and lower rainfall during other times.

In Fig. 12, the authors have divided it into five sections on an annual basis (indicated by gray dashed lines in the figure). Each of these sections is further divided into deep red, gray, and deep blue segments, representing the acceleration, steadiness, and deceleration phases, respectively. The occurrence of each period shows a certain degree of periodicity. The deep red segments, representing the accelerated phase, tends to occur during periods of rising temperatures and increased precipitation each year. With the annual temperature increase, the deformation rate gradually rises, reaching its peak usually near the annual temperature peak. It is worth noting that in the 2020 rainy season, an extreme single-day precipitation event occurred, followed by the highest deformation rates observed in nearly five years. This illustrates that precipitation has a certain accelerating effect on landslide deformation. Overall, the temperature curve and the deformation rate curve demonstrate a certain level of consistency.

Now, let's delve into a detailed analysis of these phenomena. Firstly, the study area is located in a high-altitude region of the Tibetan Plateau, where the annual maximum temperature is around 20°C, and the minimum temperature falls below 0°C. Secondly, the landslide is situated near a river, providing abundant groundwater resources. Therefore, when the temperature drops sharply each year, the soil freezes, forming permafrost. Due to the significant day-night temperature difference in the research area, permafrost persists for an extended period. As of on-site inspection on May 23, 2023, permafrost was still present. From the graph, the authors observe that the landslide deformation rate decreased in 2019 during the late rainy season of that year, despite the presence of deceleration. This is attributed to a sudden temperature drop during that period (indicated by the deep blue segment covering the temperature curve in Fig. 12). This temperature drop led to soil freezing, the formation of permafrost, causing relative ground expansion, and an increase in friction on the sliding surface, resulting in landslide deceleration. This phenomenon illustrates that the impact of temperature on the landslide is greater than that of precipitation. The remaining deep blue segments, representing the deceleration phase, are also due to the formation of permafrost caused by temperature. When temperature fluctuations occur, the landslide deformation rate shows a relatively stable state, despite minor increases due to surface permafrost thawing caused by slight temperature rises. However, these changes are short-lived due to temperature instability. Therefore, the authors categorize this period as the stability phase, represented by the gray color. It's important to note that this steadiness phase refers to a period without significant changes, but not implying that the landslide

remains entirely static. During this time, the landslide is still in a sliding state, but with a less rapid acceleration phase. Subsequently, as temperatures rise, snow melting, permafrost thawing, and increased precipitation lead to a significant rise in the landslide deformation rate, entering the acceleration phase (depicted by the deep red segment in Fig. 12). Overall, the red segments dominate most of the year, indicating that the landslide is in an accelerated downward state for most of the time. Additionally, there is a higher correlation between landslide deformation rates and temperature, with precipitation playing a supportive role in this process.

As shown in Fig. 2, there are two roads crossing the front and middle parts of the landslide area. Therefore, from Fig. 7 and Fig. 9, it can be clearly seen that larger deformation areas are predominantly distributed near the road. This is due to human engineering disturbances have a considerable disruptive effect on the slopes, and excavations on the slope create exposed surfaces. This, in turn, affects the internal stresses of the landslide mass, reducing its resistance to sliding and subsequently impacting the stability of the landslide. Therefore, human activities are also one of the significant constraints of landslide overall deformation.

From on-site investigations, the landslide exhibits a complex geological structure, influenced by both its geological composition and the previous impact of the river. The landslide deposits consist primarily consist of clayey soils with gravel content (as shown in Fig. 3e), forming thick and permeable layers. The abundant groundwater resources supplied by the river, coupled with their interaction with the soil, contribute to the degradation of the shear strength of the sliding surface materials. Consequently, the soil becomes prone to instability, leading to sliding. Additionally, there is a weakly permeable layer of fine-grained clay within the middle of the landslide body, offering some waterproofing properties. This layer has significantly higher moisture content compared to the upper and lower layers, rending it plastic and soft-plastic in nature with low shear strength, making the landslide prone to instability along this weak layer. This is also the reason why, in the slope-orientation deformation coordinate system this study constructed (Fig. 9), the movement velocity of the landslide gradually increases as the distance between the landslide and the river decreases.Therefore, in the deformation results this study obtained (Fig. 7 and Fig. 9), there is a significant deformation area near the river, which is influenced by both the river and the internal structure of the landslide mass. The combination of all these constraints mentioned above collectively contributes to the deformation of the landslide.

5.2. Spatial heterogeneity of landslide deformation

A comprehensive analysis of ascending and descending orbit InSAR deformation results (Fig. 7) indicate that the area of motion within the landslide zone is approximately 6.57×10^4 m^2 (with deformation rates exceeding 3 mm/a). So how does the landslide move? Based on the predetermined direction, it can be observed in Fig. 7 that although there are some differences between ascending and descending orbit SAR images, the deformation results indicate that most of the landslide area is moving away from the satellite, with only a portion of the rear part of the landslide moving towards the satellite. The same results are also reflected in Fig. 9, where in the slope-orientation coordinate system this study constructed, the landslide as a whole is moving downward along the average slope direction, while only a portion of the rear part of the landslide is moving in the opposite direction. Through UAV imagery (Fig. 13c), it has been discovered that the reason for this deformation pattern in the landslide is the formation of a massive depression at the rear, where the collapsing material from the surrounding area keeps accumulating into the pit. It is precisely due to the continuous accumulation of collapsing material that the predicted thickness value is relatively large in the area, which is also represented as area Ⅲ in Fig. 10.

In the obtained thickness distribution results, areas with greater activity thickness are distributed near the two roads that traverse the landslide. So why is the distribution like this? In Section 5.1, the authors discussed that the material composition of the landslide body itself and the erosion by the river in the front portion have led to the formation of significant deformation areas near the river in the front part of the landslide. Additionally, its proximity to the river has softened the sliding surface due to groundwater, reducing shear strength and weakening stability, resulting in the formation of a potential shear plane. Hence, it is not conducive to the accumulation of material at this site. So, in the thickness prediction results (Fig. 10), the thickness of the landslide mass near the river in the front part is almost zero. From the perspective of UAV (Fig. 13c), area Ⅱ and Ⅲ (Fig. 13c) are located in the middle and rear parts of the

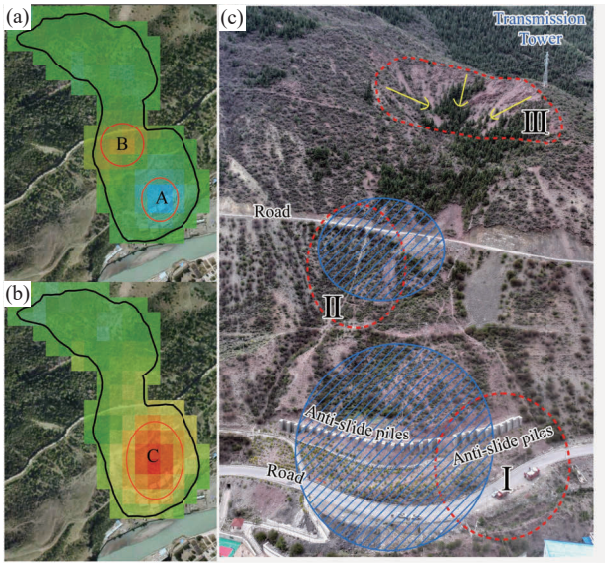

Fig. 13. Spatial heterogeneity of landslide deformation velocity fields. a–slope normal direction. b–slope direction. c–overview of study area captured by UAV. The red dashed lines in (c) correspond to area Ⅰ, area Ⅱ, and area Ⅲ in Fig. 10. The blue shaded area corresponds to regions with higher velocity of deformation in a, b.

landslide. Due to the presence of a road passing through, an excavation steep slope has been formed on the inner side of the road, creating an open surface within the shallow portion of the landslide in the middle rear areas. This has resulted in a potential shear plane, influenced by which, the inner side slope of the road has experienced collapse, and tension cracks have appeared above the road. This is why this area has a higher deformation rate and larger thickness prediction values. The steep and hilly terrain, loose soil-rock structure, and strong permeability, coupled with the widening sliding zone in the front part of the landslide and abundant water resources, have provided a basis for landslide movement and allowed for the accommodation of more material, leading to the accumulation of debris in area Ⅰ and the formation of the maximum thickness at its center. As the landslide progresses downward, the thickness gradually decreases. Through field investigations, it has been determined that this location is situated at the foot of the landslide, with nearby residential buildings and road continuously disturbing the internal structure of the slope. This constant disturbance results in changing internal stresses in the area. In addition, why do we obtain a greater thickness prediction in area Ⅰ, despite it being part of the front section of the landslide? Through field investigation and image analysis, it is evident that the landslide is situated on the convex side of the riverbank, meaning that the western side of the front section is significantly affected by river erosion, while the eastern side experiences less impact. Prolonged river erosion has resulted in the thinning of the front section while increasing the loose characteristics of the landslide material at this location. This, in turn, has allowed for the accumulation of a larger volume of material. As a result, this study obtained a higher prediction thickness value in area Ⅰ.

Further analysis reveals that in Fig. 13, area C exhibits a higher downward velocity long the slope. Consequently, it is less prone to accumulate landslide materials in this area, resulting in a smaller predicted thickness in Fig. 10. Areas A and B in Fig. 13a, on the other hand, have greater velocities in the normal direction of the slope, making them more susceptible to the accumulation of landslide materials. The positive velocity in area B indicates motion directed inward along the landslide surface, largely associated with the excavation of the road slopes, facilitating the buildup of landslide materials in this area, hence forming area Ⅱ in Fig. 13c. Area A receives landslide materials from area C, and given its greater distance from the adjacent river, it creates area Ⅰ in Fig. 13c. On the opposite side, close to the river, erosion by the river will carry away landslide materials, resulting in a smaller thickness in that area.

From the composition of the landslide, it can be inferred that this is an old landslide that has experienced reactivation due to changes in environmental conditions. Through the analysis presented above, it becomes apparent that, although the landslide is influenced by constraints such as precipitation, river dynamics, and temperature, the primary reason for the reactivation of the landslide is the disturbance caused by human engineering activities. This is evident as all the observed results are impacted by human activities. Therefore, it can be concluded that frequent human activities will undoubtedly influence the natural world.

5.3. Displacement prediction of the landslide

Predicting landslide displacement has consistently been a focal point in landslide research (Zhang L et al., 2021; Ma JW et al., 2022). Based on the study findings, the landslide in Banbar County is currently in a phase of continuous development and movement. Taking this into consideration, this study have employed the widely-used Long Short-Term Memory (LSTM) neural network model to forecast the landslide displacement. The model possesses long short-term memory (LSTM) capabilities, effectively addressing issues such as gradient vanishing and exploding. As outlined in Section 5.1, the landslide is influenced by both temperature and precipitation. Therefore, this study have curated a dataset that includes daily precipitation data during the monitoring period, displacement interpolation data from the maximum deformation point in the descending orbit results, and daily temperature data during the same time-frame. In order to ensure the model has ample data for training while maintaining the length and accuracy of the prediction sequence, this study followed the common practice in machine learning dataset partitioning, splitting the dataset in a 7∶3 ratio. Consequently, the data from August 16, 2019, to April 2, 2022, constitutes the training set, and the data from April 14, 2022, serves as the test set for predicting landslide displacement. This approach allows us to harness the power of LSTM neural networks to analyze the complex interplay of temperature, rainfall, and deformation patterns in predicting the landslide displacement, offering valuable insights for landslide monitoring and risk mitigation.

For the obtained results, the R^2 values are 0.965 (Fig. 14) and 0.996 (Fig. 15), respectively. This suggests that the predicted values based on daily temperature data and displacement interpolation data from the maximum deformation point in the descending orbit can better reflect the trend of displacement changes in this landslide. From Fig. 14, we observe a noticeable lag in the impact of precipitation on the landslide, while Fig. 15 reveals a higher correlation between temperature and landslide displacement changes. This further confirms the results from Section 5.1, where this study found that the landslide is more influenced by temperature than precipitation. Hence, the results demonstrate that the LSTM model exhibits strong capabilities in predicting the displacement of landslides that are in a continuous development and movement phase. It can effectively capture the intrinsic characteristics of the landslide, as well as the influence of external factors. Additionally, the model can achieve high accuracy in predicting landslide deformation over an extended period with a relatively short span of available data. Overall, these findings underscore the robust predictive capacity of the LSTM model for landslides,

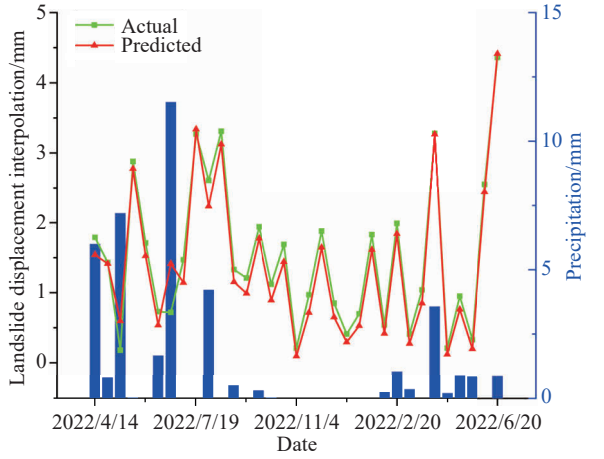

Fig. 14. Displacement prediction results based on daily precipitation data and displacement interpolation data from the maximum deformation point in the descending orbit. The green dotted line represents the actual values, the red dotted line represents the predicted values, and the blue bar graph represents the precipitation.

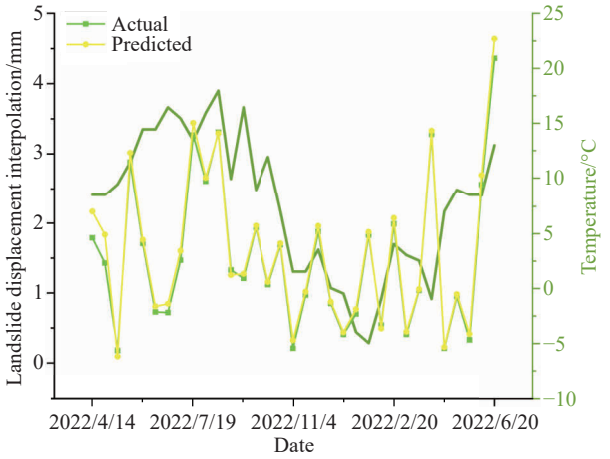

Fig. 15. Displacement prediction results based on daily temperature data and displacement interpolation data from the maximum deformation point in the descending orbit. The green dotted line represents the actual values, the yellow dotted line represents the predicted values, and the dark green dashed line represents the temperature.

highlighting its ability to reflect both the intrinsic nature of landslides and the impact of external factors, providing accurate predictions over an extended temporal scope.

5.4. Disaster prevention and mitigation considerations

Landslide disasters are a typical type of mountainous hazard in western China, resulting from a combination of internal and external factors (Zhang FY et al., 2021; Yao JM et al., 2022). Coupled with the fragile geological environment in the western region, any instability in the ecological environment can lead to significant losses. Currently, major projects such as the Sichuan-Tibet Railway and hydropower development in China have become important external drivers altering the landscape of the Tibetan mountainous region. The risk of mountainous disasters will increase as a result (Lan HX et al., 2021; Qi SW et al., 2022). Therefore, there is a need for coordinated development between engineering construction and environmental protection (Wang SJ, 1997; Wang SJ, 2002; Tian NM and Lan HX, 2022; Lan HX et al., 2022).

In this study, based on the comprehensive review of existing work and on-site investigations, it is evident that the landslide is currently in a stage of creep deformation. Based on the results of the field investigation, it obvious that anti-slide piles have been constructed locally to mitigate the landslide (Fig. 16). As shown in Fig. 16, this study have delineated area Ⅰ, area Ⅱ, and area Ⅲ from the landslide thickness prediction results using different colored shades on the UAV imagery of the landslide area. It can be observed that in area Ⅰ, despite the construction of anti-slide piles, it remains an area with significantly high predicted landslide thickness values, in other words, the construction of anti-slide piles has not effectively mitigated the movement of the landslide. According to the investigation, the landslide control project in Banbar County was completed in 2021, but during this year's (2023) field survey, it was discovered that large-scale construction activities are still ongoing near the landslide area, continuously exerting various influences on the landslide. Due to its location at the front of the landslide, being influenced by various constraints, it is advisable to reconsider the landslide safety measures for this location. Measures such as the construction of anti-slide piles, drainage ditches, and protective nets should be considered to mitigate

Fig. 16. Suggestion sites for anti-slide piles installation. Ⅰ, Ⅱ, and Ⅲ correspond to area Ⅰ, area Ⅱ, and area Ⅲ in the thickness prediction result (see Fig. 10).

the movement of the landslide. Additionally, in Section 5.1, this study can ascertain that the landslide has both a deep-seated sliding surface and shallow secondary sliding surface. As the predominant material on the shallow sliding surfaces is fine-grained clay, it possesses a certain level of waterproofing properties. Particularly, noteworthy is the abundance of rainfall in the area, which, if subjected to strong and sustained precipitation, can result in an increase in the self-weight of the landslide body, elevated pore water pressure, and a reduction in the shear strength of the sliding zone rock mass, leading to instability and deformation of the slope. If the landslide becomes unstable, it poses a risk of damage to nearby residents and roads. Furthermore, the landslide material may move down-slope, and due to the abundant water flow and high velocity in the river at the toe of the landslide, there is a risk of obstructing the river channel, potentially triggering a cascading chain of disasters and further amplifying the landslide's destructive potential. Therefore, based on the predicted landslide thickness results, it is recommended to construct anti-slide piles (as is shown in Fig. 16). Additionally, it is advisable to install protective nets in areas with steep slopes to prevent falling rocks from landing on the road, thus enhancing road safety. It is worth noting that the power transmission lines located at the rear edge of the landslide may be affected by the continuous creep of the landslide. Therefore, relevant authorities should conduct a safety assessment of the foundation of these power transmission lines to prevent potential safety issues. The specific installation depth of the anti-slide piles should be considered as a reference based on the predictive results obtained in this study. In this research, the authors used only two known thickness points as constraint conditions to inversely estimate the thickness of the entire landslide.

In this study, the authors utilized a mass conservation method to invert the landslide thickness, which is based on the assumption that the depth-averaged velocity of the landslide is a spatially constant fraction of the observed surface velocity. In assumptions, this study did not consider the volume expansion during the sliding process of the landslide (according to previous studies, this expansion rate can reach 15%–20%). Therefore, in future research, it is advisable to employ more methods and consider various variables associated with the sliding process of the landslide as much as possible. This study only estimated the overall thickness of the landslide based on two existing thickness data points, and these two points did not correspond to the maximum thickness of the landslide as per findings. Hence, in future research, efforts should be made to acquire direct observational data as much as possible to enhance the accuracy of the results. Overall, the results obtained in this study did not significantly deviate from the findings of previous field investigations, demonstrating the effectiveness of the predictive model in situations where limited information about the landslide is available.

Up to this point, the Sentinel-1 imagery employed in this study remains entirely open-source, providing continuous data support for disaster monitoring, soil conservation, urban management, and other monitoring tasks. This has accelerated the global adoption and application of InSAR technology in many countries, expediting humanity's understanding of surface geophysical phenomena (De Zan F and Monti GA, 2006; Sowter A et al., 2016; Barnhart WD et al., 2018; Raspini F et al., 2018; Lee PQ et al., 2020). Simultaneously, the prediction of landslide instability can leverage real-time monitoring data. For instance, some scholars utilize detection instruments such as ground-based synthetic aperture radar (GB-SAR), GNSS station, and more to capture real-time terrain deformation information. Subsequently, they analyze evolution stages of landslides using mathematical statistical curves, rainfall thresholds, and historical instability data from the surrounding study area to forecast future landslide development (Yin YP et al., 2010; Mirus BB et al., 2018; Xu Q et al., 2020; Yao JM et al., 2022; Zhao Z et al., 2023a).

In the future, as data availability increases, various methods will be integrated, enabling the revelation of various stages of landslide disasters, from formation to development. Moreover, future development trends for landslides and all potential risks within the study areas will be predicted.

6. Conclusions

The landslide in Banbar County is located in the geologically complex Tibetan Plateau region, where the ecological environment is extremely fragile, making it highly susceptible to damage. With the increasing intensity of development in the area, ongoing human engineering activities are perturbing the landslide. Along with fluctuations in external constraints such as precipitation and temperature, the landslide continues to experience movement. Therefore, the landslide exhibits typical characteristics of landslides in this region. This study utilizes InSAR technology in conjunction with the principles of mass conservation to analyze the deformation characteristics and potential hazards of this landslide. The following conclusions can be drawn:

(i) The results indicate that the thickness of the varies in the range of 0 to 39 m, the active area of the landslide volume is approximately 6.57×10^4 m^2, and the landslide volume is approximately 1.45×10^6 m^3. This falls into the category of a large-scale earthslide. The predictive results align closely with previous studies and on-site investigations, further confirming the reliability of this method. However, it should be noted that this study constrained the entire thickness of the landslide based on just two known data points, and these two points are not located in areas with larger predicted thickness values. Therefore, it is essential to conduct on-site surveys in study area with larger predicted thickness values to further validate the accuracy of this study's findings and implement additional methodological measures in subsequent research.

(ii) The spatio-temporal patterns of landslide deformation is controlled by the complex internal structure of the landslide mass and its interaction with constraints such as precipitation, temperature, and human activities. The landslide continues to

be in a state of movement influenced by these constraints. Overall, the deformation rate of the landslide primarily exhibits periodic variations in response to temperature changes within the study area. The maximum deformation rates of the landslide occur in proximity to the highest annual temperatures, typically corresponding to the acceleration phase of the landslide. Precipitation has a certain promoting effect on this phase. As temperatures decrease, due to the unique geographical location of the study area, the landslide transitions into a deceleration deformation phase. During other times, the deformation rate of the landslide fluctuates in accordance with temperature fluctuations, representing a steadiness phase. Human activities have a considerable influence on the spatio-temporal patterns of landslide deformation, with several prominent deformation areas directly influenced by human interventions. Therefore, reducing the impact of human activities on the natural environment and achieving harmony between humans and nature is the key to achieving sustainable development and ecological balance on Earth.

(iii) The displacement of landslides was predicted using an LSTM neural network model. The results indicate that temperature has a greater impact on this landslide than precipitation, and there is a certain lag in the effect of precipitation on landslide deformation. The findings highlight the LSTM model's strong predictive capability for the development of landslide displacement during the creep phase, showcasing its ability to reflect both the intrinsic characteristics of landslides and the influence of external factors. The model can provide accurate predictions over an extended time range.

(iv) Based on the spatial heterogeneity of landslide deformation, new considerations have been proposed for the prevention and mitigation of landslide disasters: constructing new anti-slide piles in the central part of the landslide; increasing protective nets appropriately to prevent falling debris; conducting safety inspections on the transmission towers and electricity poles affected by the landslide. Additionally, the anti-slide piles built in 2021 did not have a significant mitigating effect, which may be related to ongoing human activities at the front of the landslide. Therefore, safety measures at this location should be reevaluated, such as reconstructing anti-slide piles, increasing drainage ditches, and installing protective nets. This landslide is continuously perturbed and may face instability in the future. Increasing awareness of potential hazards, implementing safety measures, and reducing the impact of human activities on the environment are critical issues at present.

CRediT authorship contribution statement

Guan-hua Zhao, Heng-xing Lan, Lang-ping Li, Hui-yong Yin, Alexander Strom, Wei-feng Sun, Chao-yang Tian conceived of the presented idea. Guan-hua Zhao, Lang-ping Li carried out the experiment. All authors discussed the results and contributed to the final manuscript.

Declaration of competing interest

The authors declare no conflicts of interest.

Acknowledgment

This study is supported by the second Tibetan Plateau Scientific Expedition and Research (STEP) program (Grant NO. 2019QZKK0904), the National Natural Science Foundation of China (Grant No. 41941019), and the National Natural Science Foundation of China (Grant NO. 42307217).

References

Aryal A, Brooks BA, Reid ME. 2015. Landslide subsurface slip geometry inferred from 3-D surface displacement fields. Geophysical Research Letters, 42(5), 1411–1417. doi: 10.1002/2014gl062688.

BISHOP KM. 1999. Determination of translational landslide slip surface depth using balanced cross sections. Environmental & Engineering Geoscience, 5(2), 147–156. doi: 10.2113/gseegeosci.V.2.147.

Bichler A, Bobrowsky P, Best M, Douma M, Hunter J, Calvert T, Burns R. 2004. Three-dimensional mapping of a landslide using a multi-geophysical approach: The Quesnel Forks landslide. Landslides, 1(1), 29–40. doi: 10.1007/s10346-003-0008-7.

Booth AM, Lamb MP. Avouac JP, Delacourt C. 2013. Landslide velocity, thickness, and rheology from remote sensing: La Clapière landslide, France. Geophysical Research Letters, 40(16), 4299–4304. doi: 10.1002/grl.50828.

Booth AM, Roering JJ, Rempel AW. 2013. Topographic signatures and a general transport law for deep-seated landslides in a landscape evolution model(Article). Journal of Geophysical Research:Earth Surface, 118(2), 603–624. doi: 10.1002/jgrf.20051.

Barnhart WD, Yeck WL, McNamara DE. 2018. Induced earthquake and liquefaction hazards in Oklahoma, USA: Constraints from InSAR. Remote Sensing of Environment, 218(0), 1–12. doi: 10.1016/j.rse.2018.09.005.

Coe JA, Ellis WL, Godt JW, Savage WZ, Savage JE, Michael JA, Kibler JD, Powers PS, Lidke DJ, Debray S. 2003. Seasonal movement of the Slumgullion landslide determined from Global Positioning System surveys and field instrumentation, July 1998–March 2002. Engineering Geology, 68(1–2), 67. doi: 10.1016/s0013-7952(02)00199-0

CVX Research, Inc. 2013, CVX: Matlab software for disciplined convex programming, version 2.0 beta., edited.

Cigna F, Bateson LB, Jordan CJ, Dashwood C. 2014. Simulating SAR geometric distortions and predicting Persistent Scatterer densities for ERS-1/2 and ENVISAT C-band SAR and InSAR applications: nationwide feasibility assessment to monitor the landmass of Great Britain with SAR imagery. Remote Sensing of Environment, 152, 441–466. doi: 10.1016/j.rse.2014.06.025.

Chen XZ, Cui YF. 2017. The formation of the Wulipo landslide and the resulting debris flow in Dujiangyan City, China. Journal of Mountain Science, 14(6), 1100–1112. doi: 10.1007/s11629-017-4392-1.

Cao YM, Guo W, Wu YM, Li LP, Zhang YX, Lan HX. 2022. An hourly shallow landslide warning model developed by combining automatic landslide spatial susceptibility and temporal rainfall threshold predictions. Journal of Mountain Science, 19(12), 3370–3387. doi: 10.1007/s11629-022-7370-1.

De Zan F, Guarnieri AM. 2006. TOPSAR: Terrain observation by progressive scans(Article). IEEE Transactions on Geoscience and Remote Sensing, 44(9), 2352–2360. doi: 10.1109/tgrs.2006.873853.

Delacourt C, Allemand P, Berthier E, Raucoules D, Casson B, Grandjean P, Pambrun C, Varel E. 2007. Remote-sensing techniques for

analysing landslide kinematics: A review. Bulletin de la Société Géologique de France, 178(2), 89–100. doi: 10.2113/gssgfbull.178.2.89.

Dai KR, Zhang LL, Song C, Li ZH, Zhuo GC, Xu Q. 2021. Quantitative analysis of Sentinel-1 imagery geometric distortion and their suitability along Sichuan-Tibet Railway. Geomatics and Information Science of Wuhan University, 46(10), 1450–1460. doi: 10.13203/j.whugis20210130.

Esposito C, Natale A, Palmese G, Berardino P, Perna S. 2019. Geometric distortions in FMCW SAR images due to inaccurate knowledge of electronic radar parameters: Analysis and correction by means of corner reflectors. Remote Sensing of Environment, 232, 111289. doi: 10.1016/j.rse.2019.111289.

Feigl KL, Dupré E. 1999. RNGCHN: A program to calculate displacement componenets from dislocations in an elastic half-space with applications for modeling geodetic measurements of crustal deformation. Computers & Geosciences, 25(6), 695–704. doi: 10.1016/s0098-3004(99)00003-5.

Farinotti D, Huss M, Bauder A, Funk M, Truffer M. 2009. A method to estimate the ice volume and ice-thickness distribution of alpine glaciers. Journal of Glaciology, 55(191), 422–430. doi: 10.3189/002214309788816759.

Fan XM, Xu Q, Scaring, G, Dai LX, Li WL, Dong XJ, Zhu X, Pei XJ, Dai KR, Havenith HB. 2017. Failure mechanism and kinematics of the deadly June 24th 2017 Xinmo landslide, Maoxian, Sichuan, China. Landslides, 14(6), 2129–2146. doi: 10.1007/s10346-017-0907-7.

Fan XM, Xu Q, Alonso-Rodriguez A, Subramanian SS, Li WL, Zheng G, Dong XJ, Huang RQ. 2019. Successive landsliding and damming of the Jinsha River in eastern Tibet, China: Prime investigation, early warning, and emergency response. Landslides, 16(5), 1003–1020. doi: 10.1007/s10346-019-01159-x.

Feng WK, Yi XY, Ge H, Wang Q, Li ZG, Zhan GX. 2017. In-situ borehole shear tests on cataclastic rock mass of Daguangbao landslide(Article). Yantu Gongcheng Xuebao/Chinese Journal of Geotechnical Engineering, 39(9), 1718–1723. doi: 10.11779/cjge201709021.

Froude MJ, Petley DN. 2018. Global fatal landslide occurrence from 2004 to 2016(Article). Natural Hazards and Earth System Sciences, 18(8), 2161–2181. doi: 10.5194/nhess-18-2161-2018.

Ge DQ. 2018. Comprehensive remote sensing applications in early detection, monitoring, and warning of geological disasters. City and Disaster Reduction, 6, 53–60 (in Chinese with English abstract).

He KS, Zhang WM, Wang GQ, Jia XT. 2005. Ground penetrating radar application research for dam landslide disasters. Advances in Science and Technology of Water Resources, 2, 36–39 (in Chinese with English abstract).

Hu X, Wang T, Pierson TC, Lu Z, Kim J, Cecere TH. 2016. Detecting seasonal landslide movement within the Cascade landslide complex (Washington) using time-series SAR imagery. Remote Sensing of Environment, 187, 49–61. doi: 10.1016/j.rse.2016.10.006.

Huang MH, Fielding EJ, Liang C, Milillo P, Bekaert D, Dreger D, Salzer J. 2017. Coseismic deformation and triggered landslides of the 2016 Mw 6. 2 Amatrice earthquake in Italy. Geophysical Research Letters, 44(3), 1266–1274. doi: 10.1002/2016gl071687.

Hu X, Lu Z, Pierson T, Kramer R, George D. 2018. Combining InSAR and GPS to determine transient movement and thickness of a seasonally active low-gradient translational landslide. Geophysical Research Letters, 45(3), 1453–1462. doi: 10.1002/2017gl076623.

Handwerger AL, Booth AM, Huang MH, Fielding EJ. 2021. Inferring the Subsurface Geometry and strength of slow-moving landslides using 3-D velocity measurements from the NASA/JPL UAVSAR. Journal of Geophysical Research: Earth Surface, 126(3). doi: 10.1029/2020jf005898

Kovács IP, Bugya T, Czigány S, Defilippi M, Lóczy D, Riccardi P, Ronczyk L, Pasquali P. 2019. How to avoid false interpretations of Sentinel-1A TOPSAR interferometric data in landslide mapping? A case study: Recent landslides in Transdanubia, Hungary. Natural Hazards, 96(2), 693. doi: 10.1007/s11069-018-3564-9.

Kang Y, Lu Z, Zhao CY, Qu W. 2023. Inferring slip-surface geometry and volume of creeping landslides based on InSAR: A case study in Jinsha River basin. Remote Sensing of Environment, 294, 113620. doi: 10.1016/j.rse.2023.113620.

Liao MS, Zhang L, Shi XG. 2017. Methods and Practices of Landslide Deformation Radar Remote Sensing Monitoring. Beijing, Science Press, 1-186 (in Chinese).

Lee PQ, Xu L, Clausi DA. 2020. Sentinel-1 additive noise removal from cross-polarization extra-wide TOPSAR with dynamic least-squares. Remote Sensing of Environment, 248, 111982. doi: 10.1016/j.rse.2020.111982.

Lan HX, Zhang N, Li LP, Tian NM, Ji YX, Liu SJ, Li G, Tian CY, Wu YM, Yao JM, Peng JB, Zhou CH. 2021. Risk analysis of major engineering geological hazards for Sichuan-Tibet Railway in the phase of feasibility study. Journal of Engineering Geology, 29(2), 0326–16 (in Chinese with English abstract). doi: 10.13544/j.cnki.jeg.2021-0114.

Lan HX, Tian NM, Li LP, Wu YM, Macciotta R, Clague JJ. 2022. Kinematic-based landslide risk management for the Sichuan-Tibet Grid Interconnection Project (STGIP) in China. Engineering Geology, 308, 106823. doi: 10.1016/j.enggeo.2022.106823.

Li LP, Lan HX, Strom A, Macciotta R. 2022. Landslide length, width, and aspect ratio: Path-dependent measurement and a revisit of nomenclature. Landslides, 19(12), 3009–3029. doi: 10.1007/s10346-022-01935-2.

Morlighem M, Rignot E, Seroussi H, Larour E, Dhia HB, Aubry D. 2011. A mass conservation approach for mapping glacier ice thickness. Geophysical Research Letters, 38(19). doi: 10.1029/2011gl048659.

Mirus BB, Becker RE, Baum RL, Smith JB. 2018. Integrating real-time subsurface hydrologic monitoring with empirical rainfall thresholds to improve landslide early warning. Landslides, 15(10), 1909–1919. doi: 10.1007/s10346-018-0995-z.

Ma JW, Xia D, Guo HX, Wang YK, Niu XX, Liu ZY, J S. 2022. Metaheuristic-based support vector regression for landslide displacement prediction: A comparative study. Landslides, 19(10), 1–23. doi: 10.1007/s10346-022-01923-6.

Nikolaeva E, Walter TR, Shirzaei M, Zschau J. 2014. Landslide observation and volume estimation in central Georgia based on L-band InSAR(Article). Natural Hazards and Earth System Sciences, 14(3), 675–688. doi: 10.5194/nhess-14-675-2014.

Qiu HJ, Cui P, Regmi AD, Hu S, Wang XG, Zhang YZ, He Y. 2017. Influence of topography and volume on mobility of loess slides within different slip surfaces. CATENA, 157(2), 180–188. doi: 10.1016/j.catena.2017.05.026.

Qi SW, Li YC, Song SH, Lan HX, Ma FS, Li ZQ, Chen XQ, Cui ZD, Zhang LQ, Liu CL, Chen WZ, Zou Y, Tang FJ, Lu X, Guo SF. 2022. Regionalization of engineering geological stability and distribution of engineering disturbance disasters in Tibetan Plateau. Journal of Engineering Geology, 30(3), 599–608 (in Chinese with English abstract). doi: 10.13544/j.cnki.jeg.2022-0172.

Rasmussen LA, Lowell A. 1988. Bed topography and mass-balance distribution of Columbia Glacier, Alaska, USA, determined from sequential aerial photography. Journal of Glaciology, 34(117), 208–216. doi: 10.1017/s0022143000032251.

Rowan MG, Kligfield R. 1989. Cross section restoration and balancing as aid to seismic interpretation in extensional terranes. AAPG Bulletin, 73(8), 955–966. doi: 10.1306/44b4a2bc-170a-11d7-8645000102c1865d.

Raspini F, Bianchini S, Ciampalini A, Soldato MD, Solari L, Novali F, Conte SD, Rucci A, Ferretti A, Casagli N. 2018. Continuous, semi-automatic monitoring of ground deformation using Sentinel-1 satellites. Scientific Reports, 8(1), 7253. doi: 10.1038/s41598-018-25369-w.

Sassa K, Yin Y, Canuti P. 2015. The third world landslide forum, Beijing, 2014. Landslides, 12(1), 177–192. doi: 10.1007/s10346-015-0555-8.

Sun Q, Hu J, Zhang L, Ding XL. 2016. Towards slow-moving landslide monitoring by integrating multi-sensor InSAR time series datasets: The Zhouqu Case Study, China. Remote Sensing, 8(11), 908. doi: 10.3390/rs8110908.

Sowter A, Bin Che Amat M, Cigna F, Marsh S, Athab A, Alshammari L. 2016. Mexico City land subsidence in 2014–2015 with Sentinel-1 IW TOPS: Results using the Intermittent SBAS (ISBAS) technique. International Journal of Applied Earth Observation and Geoinformation, 52, 230–242. doi: 10.1016/j.jag.2016.06.015.

Shi GL, Chen Q, Liu XW, Yang YH, Xu Q, Zhao JJ. 2022. Deformation velocity field along aspect direction of an ancient landslide at Taoping village derived from ascending and descending Sentinel-1A data. Journal of Engineering Geology, 30(4), 1350–1361 (in Chinese with English abstract).

Tian NM, Lan HX. 2022. The indispensable role of resilience in rational landslide risk management for social sustainability. Geography and Sustainability, 4(1), 70–83. doi: 10.1016/j.geosus.2022.11.007.

Wang SJ. 1997. Interaction between human engineering activity and geoenvironment and its environment effects. Journal of Geological Hazards and Environment Preservation, 8(1), 19–26 (in Chinese with English abstract).

Wang SJ. 2002. Coupling of earth's endogenic and exogenic geological processes and progins on serious geological disasters. Journal of Engineering Geology, 2, 115–117 (in Chinese with English abstract).

Xu, Q, Peng DL, Zhang S, Zhu X, He CY, Qi X, Zhao KY, Xiu DH, Ju, NP. 2020. Successful implementations of a real-time and intelligent early warning system for loess landslides on the Heifangtai terrace, China. Engineering Geology, 278(0), 105817. doi: 10.1016/j.enggeo.2020.105817.

Yang YF, Zhang ZH, Fu J. 2009. Detection of GPR and determination of district and depth on landslide area. Journal of Zhejiang Sci-Tech University, 3, 395–398 (in Chinese with English abstract).

Yin YP, Wang HD, Gao YL, Li XC. 2010. Real-time monitoring and early warning of landslides at relocated Wushan Town, the Three Gorges Reservoir, China. Landslides, 7(3), 339–349. doi: 10.1007/s10346-010-0220-1.

Yang G, Shu ZP, Zhang J, Deng R. 2021. Development features and disaster prevention study of a landslide in Bianba County, Changdu City, Tibet. Resource Information and Engineering, 36 (5), 118–122 (in Chinese with English abstract). doi: 10.19534/j.cnki.zyxxygc.2021.05.034.

Yao JM, Lan HX, Li LP, Cao YM, Wu YM, Zhang YX, Zhou CD. 2022. Characteristics of a rapid landsliding area along Jinsha River revealed by multi-temporal remote sensing and its risks to Sichuan-Tibet railway. Landslides, 19(3), 703–718. doi: 10.1007/s10346-021-01790-7.

Yang C, Yang YH, Wang JY, Xu Q, Chen Q, Tao XX, Hu ZQ. 2023. Inferring landslide depth based on ascending and descending InSAR deformations-example of Taoping village ancient landslide. Journal of Engineering Geology, 31(3), 868–879 (in Chinese with English abstract). doi: 10.13544/j.cnki.jeg.2021-0172.

Zhang T, Fang XM, Song CH, Appel E, Wang YD. 2014. Cenozoic tectonic deformation and uplift of the South Tian Shan: Implications from magnetostratigraphy and balanced cross-section restoration of the Kuqa depression. Tectonophysics, 628, 172–187. doi: 10.1016/j.tecto.2014.04.044.

Zhou L, Guo JM, Hu JY, Li JW, Xu YF, Pan YJ, Shi M. 2017. Wuhan surface subsidence analysis in 2015–2016 based on Sentinel-1A Data by SBAS-InSAR. Remote Sensing, 9(10), 982. doi: 10.3390/rs9100982.

Zhao CY, Lu Z. 2018. Remote sensing of landslides—A review. Remote Sensing, 10(2), 279. doi: 10.3390/rs10020279.

Zhu Q, Zeng HW, Ding YL, Xie X, Liu F, Zhang LG, Li HF, Hu H, Zhang JX, Chen L, Chen L, Zhang PC, He HG. 2019. A review of major potential landslide hazards analysis. Acta Geodaetica et Cartograpgica Sinica, 48(12), 1551–1561. doi: 10.11947/j.AGCS.2019.20190452.

Zhang YS, Liu XY, Yao X. 2020. InSAR-based method for early recognition of ancient landslide reactivation in Dadu River, China. Journal of Hydraulic Engineering, 51(5), (in Chinese with English abstract). doi: 10.13243/j.cnki.slxb.20200034

Zhang L, Shi B, Zhu HH, Han HM, Fan XD. 2021. PSO-SVM-based deep displacement prediction of Majiagou landslide considering the deformation hysteresis effect. Landslides, 18(1), 179–193. doi: 10.1007/s10346-020-01426-2.

Zhao Z, Chen JH, Xu KH, Xie HW, Gan XX, Xu H. 2021. A spatial case-based reasoning method for regional landslide risk assessment. International Journal of Applied Earth Observation and Geoinformation, 102, 102381. doi: 10.1016/j.jag.2021.102381.

Zhang FY, Peng JB, Huang XW, Lan HX. 2021. Hazard assessment and mitigation of non-seismically fatal landslides in China. Natural Hazards, 106(1), 785–804. doi: 10.1007/s11069-020-04491-x.

Zhu W, Yang LY, Zhang JM, Li ZH, Xu XY. 2023. Thickness estimation of Xiongba landslide in Gongjue area of Tibet, China by combining InSAR and mass conservation method. Journal of Earth Sciences and Environment, 45(3), 535–547 (in Chinese with English abstract). doi: 10.19814/j.jese.2022.12081.

Zhao Z, Chen JH, Yao JM, Xu KH, Liao YY, Xie HW, Gan XX. 2023a. An improved spatial case-based reasoning considering multiple spatial drivers of geographic events and its application in landslide susceptibility mapping. Catena, 223, 106940. doi: 10.1016/j.catena.2023.106940.

Zhao Z, Chen JH. 2023b. A robust discretization method of factor screening for landslide susceptibility mapping using convolution neural network, random forest, and logistic regression models. International Journal of Digital Earth, 16(1), 408–429. doi: 10.1080/17538947.2023.2174192.

Zhao Z, Lan HX, Li LP, Strom A. 2024. Landslide spatial prediction using cluster analysis. Gondwana Research. 130, 291– 307. doi: 10.1016/j.gr.2024.02.006